Hindawi
Advances in Materials Science and Engineering
Volume 2023, Article ID 3008695, 22 pages
https://doi.org/10.1155/2023/3008695

Research Article

Research on the Stress and Deformation Characteristics of Circular Foundation Pit during Excavation in Sand Soil

Xuhe Gao,[1,2] **Weiping Tian**,[3] **Jiachun Li**,[3] **Hongliang Qi**,[3] **Shiyang Li**,[1] **and Zhipei Zhang**[4]

[1]*School of Mechanics,Civil Engineering and Architecture, Northwestern Polytechnical University, Xi'an, Shaanxi 710129, China*
[2]*Observation and Research Station of Ground Fissure and Land Subsidence, Ministry of Natural Resources, Xi'an, Shaanxi 710054, China*
[3]*Key Laboratory of Highway Engineering in Special Region, Ministry of Education, Chang'an University, Xi'an, Shaanxi 710064, China*
[4]*College of Geology and Environment, Xi'an University of Science and Technology, Xi'an, Shaanxi 710054, China*

Correspondence should be addressed to Xuhe Gao; 81706037@qq.com

Received 7 October 2022; Revised 28 December 2022; Accepted 9 January 2023; Published 18 January 2023

Academic Editor: Sheraz Ahmad

The stress and deformation response characteristics of the support structure in the process of excavation and support of circular sand foundation pit are complex. The existing research results lack a general analysis method for the mutual check between the field monitoring data and the numerical simulation results. This research relies on the excavation and support project of a circular foundation pit in the sandy soil layer of the west anchorage of Humen Second Bridge. The force and deformation characteristics of foundation pit soil are monitored and structure is supported during construction. A new method for checking simulation parameters based on the excursion monitoring data of the diaphragm wall is proposed. The modeling and calculation theory of foundation pit excavation and support process is established. The superposition calculation of pore water pressure is used to realize the foundation pit seepage-stress coupling. The effects of steady-state seepage conditions on the equivalent strain of foundation pit soil, the displacement of the diaphragm wall, and the axial force of the lining are compared and analyzed. The stress and deformation mechanism of the soil layer and supporting structure during the excavation and support of a circular foundation pit in the sand layer is obtained.

1. Introduction

Circular foundation pits are strong and have clear spatial effects. However, these foundation pits are often built next to riverbanks, which pose challenges for designing and safely constructing these structures. Accordingly, the design and construction of circular foundation pits have attracted the attention of many engineers and researchers [1–4]. For example, Faheem et al. [5] used the finite element method to study the stability of rectangular foundation pits. Dai et al. [6] used models of underground diaphragm walls and found that these structures experience overall tilt failure under horizontal force. Wang [7] investigated wide, narrow, and general foundation pits, as determined by the ratio of the foundation pit width to the insertion depth of the supporting structure, and subsequently derived formulae for calculating the appropriate factor of safety to prevent overturning in each type of foundation pit. Although there has been some discussion regarding the overall stability of supporting structures for circular foundation pits, most analyses rely on plane assumptions based on flat site conditions [8–12]. Thus, the effects of complex site conditions, such as adjacent river channels and sandy soil layers, on the stability of circular foundation pits remain to be studied. Specifically, there is a lack of research on the force and deformation characteristics of the foundation pit supporting structure in complex settings.

In addition to the baseline conditions of a site, rainfall during construction can have a significant impact on the

safety of a foundation pit project. This is especially the case for foundation pits constructed in complex soil conditions where the soil has high water content and low shear strength. In such cases, the force distribution and deformation of the soil are easily affected by the conditions of the external environment. To date, there have been few studies on the mechanism of force and deformation response of circular foundation pit excavation and support based on monitoring data, checking parameters, and stress-seepage coupling. Most of the existing research results focus on the influence of groundwater on the deformation of foundation pits with common structures [13–17]. Some studies have focused on the effect of rainfall on unsaturated soil slopes, while others have investigated the deformation and stability of foundation pits under rainfall conditions. For example, Li et al. [18] used finite element numerical calculations in ABAQUS software to analyze the stability of a foundation pit slope under rainfall conditions.

During the excavation of a circular foundation pit, the selection of calculation parameters in the theoretical analysis and numerical simulation of the foundation pit has a great influence on the results of stress and deformation. Existing parameter of the selection methods focusses on probabilistic inverse analysis. The field practicability of the research results is poor, and there is a lack of a parameter checking method that can link field monitoring and numerical simulation [19–21]. Therefore, it is of great theoretical and practical significance to propose and establish a new method for parameter checking, and to carry out research on the deformation response mechanism of deep soil under circular foundation pit excavation and support.

This study investigates the force and deformation characteristics of the support structure during the excavation of a circular foundation pit in a sand layer before and after considering seepage conditions. On the basis of previous work, a research method combining on-site monitoring and numerical simulation research is adopted. The stress-seepage coupling is realized using the superposition calculation method of pore water pressure. Explore and propose a new method for dynamic verification of numerical simulation parameters based on monitoring data. Finally, the force and deformation law of the supporting structure during the excavation of the circular foundation pit is analyzed.

2. Materials and Methods

2.1. Study Area and Foundation Pit Parameters. The cover layer of the soil in the study area is mainly composed of Quaternary Holocene sea-land alternate facies silt, silty soil, sandy soil, Quaternary Pleistocene silty clay, sandy soil, and pebble soil. The cover layer is 24.20–28.50 m thick, and the basement layer is made of chalk. The base of the cover layer is composed of mudstone from the BAIHEDONG Formation (K1b), with uneven weathering and weathered interlayer phenomena. Stable and continuous moderately weathered rocks as well as slightly weathered rocks are variably spaced and buried from approximately 32.10 m to 52.00 m below the surface. A cross-sectional view of the study area is shown in Figure 1.

The groundwater in the study area is composed primarily of Quaternary pore confined water and some bedrock fissure confined water. In our modeling, we considered silt, silty clay, residual soil, and fully weathered rock to form a relatively impermeable aquifer and water-proof layer. The sand gravel layer was considered the main water storage layer, though groundwater in the area is relatively shallow. The underlying mudstone has developed weathered fissures; however, its occurrence is limited. Thus, the water permeability in this layer is very limited.

With regards to the foundation pit and support structure, the outer diameter of the diaphragm wall is 82.0 m, the wall thickness is 1.5 m, and the bottom of the wall is embedded in argillaceous siltstone and moderately weathered mudstone. The construction trough section of the diaphragm wall is divided into phase I and phase II, which are composed of 27 trough sections each. The maximum designed groove depth is 46.0 m. A schematic of the foundation pit support structure is shown in Figure 2.

After the construction of the diaphragm wall was completed, the top-down method was used to excavate the soil layer by layer; the lining of the foundation pit was also constructed in layers. The construction of each layer was dictated by the excavation of the soil. The soil was excavated to a depth of 27 m, and the height of the lining and soil layering was controlled within 3 m. The inner lining had an inner thickness of 1.5 m from 0 to 6 m deep and a thickness of 2 m below 6 m deep. The top and bottom plates were 6 m thick. The foundation pit layers are shown in Figure 3.

2.2. Monitoring the Horizontal Displacement of the Diaphragm Wall. Based on the characteristics of the circular foundation pit, 8 hollow PVC plastic pipes with guide grooves (labeled P1–P8) were evenly arranged around the diaphragm wall, as shown in Figure 4. The side hole tracks the lateral displacement of the enclosure structure, and the measurement depth is the same as the wall depth. A total of 12 inclinometer tubes were also arranged around the foundation pit at P1–P8, with additional inclinometer holes (P1′, P3′, P5′, and P7′) located in the slot section identical to P1, P3, P5, and P7.

The underground diaphragm wall is divided into 54 trough sections; for simplicity, the wall offset data corresponding to trough Sections 2 (P1), 15 (P3), 28 (P5), and 42 (P7) were selected for analysis. In the subsequent simulation of working conditions, the direction of the calculation result is defined according to the direction of the trough sections.

During the excavation of the foundation pit, a number of monitoring projects such as the displacement of the diaphragm wall, the displacement of the ground surface and the pore water pressure were carried out. Due to the limitations of the installation of measuring points and the actual situation of construction, the displacement of the diaphragm wall is almost the only monitoring project that can collect the data of the whole life cycle of the foundation pit. Therefore, this study selects the diaphragm wall as the parameter checking standard.

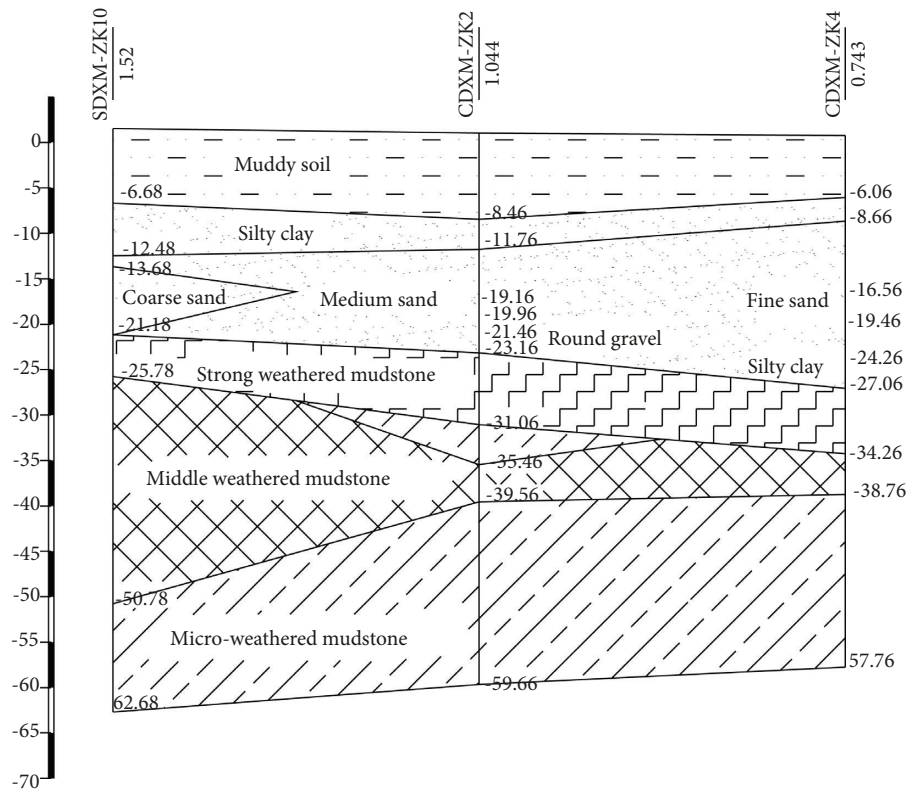

Figure 1: Cross-sectional view along the bridge of the geological features in the study area.

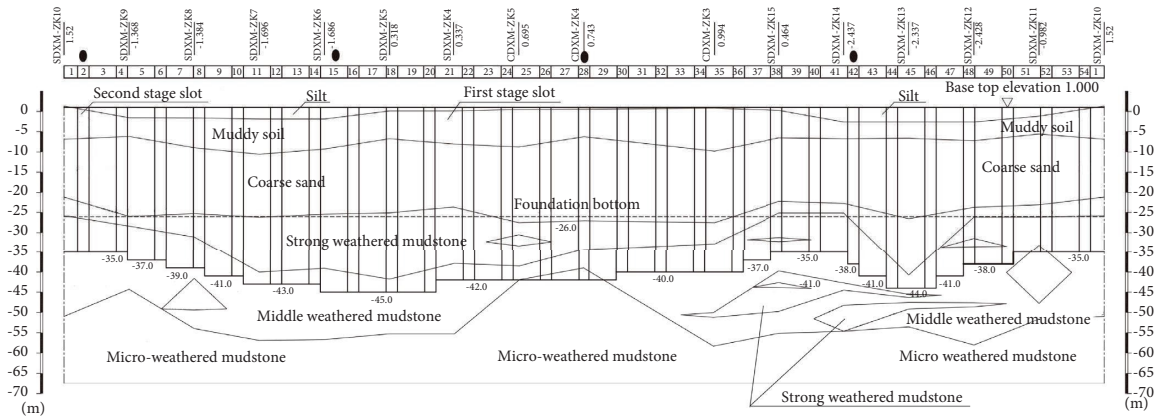

Figure 2: Slot expansion view.

2.3. Development of the Numerical Simulation Model

2.3.1. Simulation Assumptions and Regions. Midas/GTS NX software is selected for modeling. The simulation assumptions were as follows:

(1) The rock and soil of the foundation pit obey Mohr–Coulomb's strength yield criterion

(2) The influence of groundwater on the foundation pit can be simplified as a steady flow

(3) Each structural unit in the underground diaphragm wall and inner lining is completely elastic

The calculation model was defined to be 300 m long, 300 m wide, and 100 m deep. The soil layers of the foundation pit model were defined from top to bottom as follows: 0–3 m deep silt, 3–6 m deep silty clay, 6–12 m deep silt sand, 12–18 m deep medium sand, 18–24 m deep coarse sand, 24–40 m deep strongly weathered mudstone, 40–70 m deep medium weathered mudstone, and 70–100 m deep slightly weathered mudstone. The bottom end of the underground diaphragm wall is embedded in weathered mudstone, and the embedded depth is 10–20 m. The lining of the pit was 1.5 m thick from 0 to 6 m deep and 2 m thick below 6 m deep.

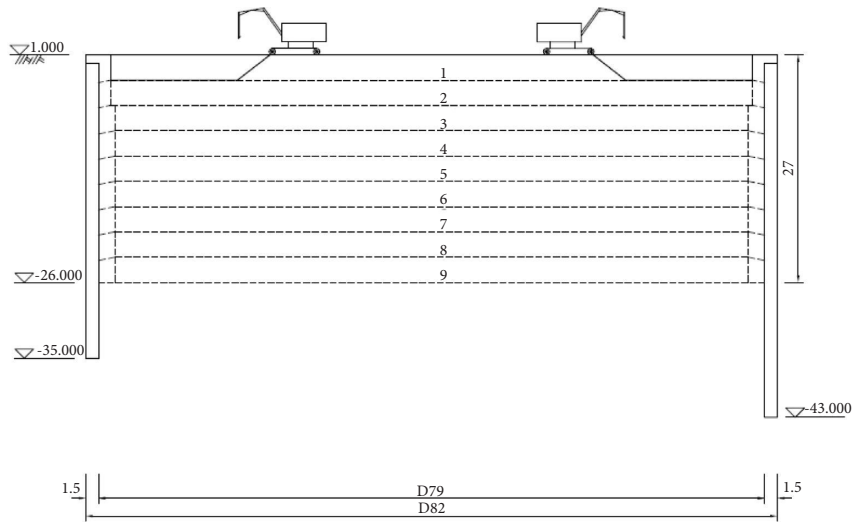

Figure 3: Elevation view of the foundation pit excavation layers.

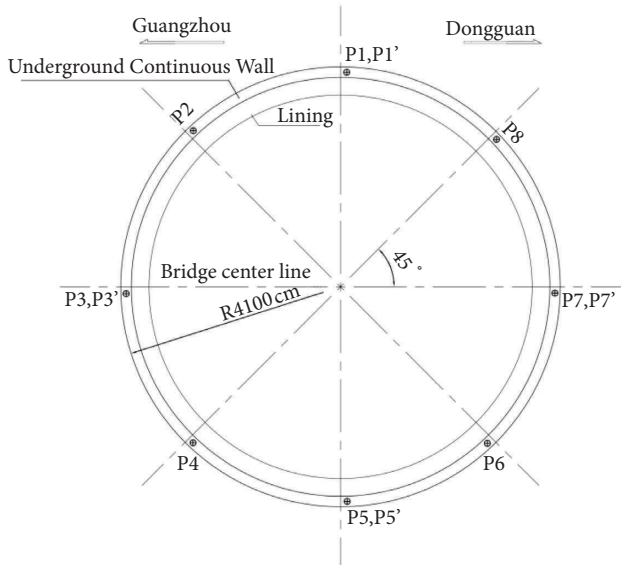

Figure 4: Deep deformation monitoring points for the diaphragm wall.

The model default contact parameters: the normal stiffness scaling factor is 1, and the tangential stiffness scaling factor is 0.1. At the same time, adjust the auxiliary nodes to eliminate internal penetration.

The rock and soil layer is controlled by entity attributes in the model, the grid is divided into 10 m in the XY plane, and the Z direction is divided according to the thickness of the rock and soil layer. The lining is controlled by line property in the model, and the section size is 1.5 m × 3.0 m. The underground diaphragm wall is controlled by plane attribute in the model, and the thickness is 1.5 m. The thermal expansion coefficient of reinforced concrete constituting the inner lining and underground diaphragm wall is $1e-006$, and the damping ratio is 0.05.

Lining and diaphragm walls, diaphragm walls, and geotechnical layers are connected by default contact parameters.

The errors of foundation pit excavation construction conditions are controlled by on-site construction monitoring, and the modeling results are adjusted by parameter checking. Finally, the subsequent working conditions are analyzed according to the calculation results.

2.3.2. Model Boundary Conditions. The boundary conditions for the numerical model are as follows:

(1) The left and right boundaries of the model are constrained in the X-direction, with $u = 0$, where u is the displacement in the X-direction, v is the displacement in the Y-direction, and w is the displacement in the Z-direction

(2) The front and back boundaries of the model are constrained in the Y-direction, with $v = 0$

(3) The bottom boundary of the model is a fully constrained boundary, with $u = v = w = 0$

(4) The upper boundary of the model is defined as a free boundary; thus, no constraints are given

(5) The initial stress is the self-weight stress of the formation

Based on the abovementioned conditions, a model with a length, width, and height of $300 \times 300 \times 100$ m was established, with a total of 15,840 units and 50,588 calculation equations (Figure 5). The meshing model of the underground diaphragm wall and lining structure is shown in Figure 6.

2.3.3. Model Parameter Validation. The existing methods for selecting simulation parameters for modeling foundation pit excavation include using parameters obtained through geotechnical tests, relying on statistical data selected from projects with similar conditions, and using empirical data. However, each of these approaches has limitations. The parameters obtained from geotechnical tests need to be corrected for use in simulation calculations, whereas

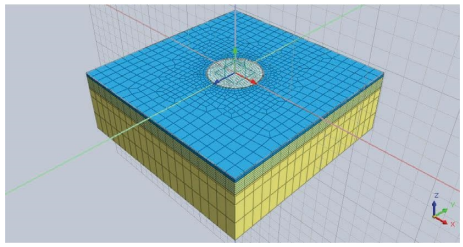

Figure 5: Grid diagram of the pit model.

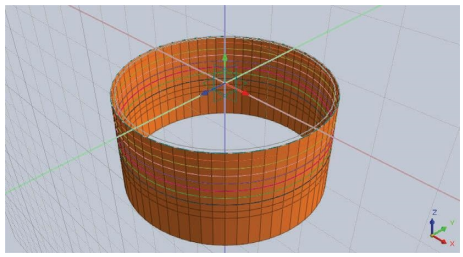

Figure 6: Grid diagram of the support structure (diaphragm wall and lining).

parameters selected from statistical data are only applicable to ordinary stratum and requires the accumulation of data from many engineering projects. Furthermore, empirical data are convenient to use, but lacks in scientific rigor. Significantly, none of these methods are universally applicable. Thus, the depth displacement monitoring data and P value check are used to verify the c (Cohesion), φ (Friction angle), and E (Elastic Modulus) values of the foundation pit rock and soil (Under the Mohr–Coulomb elastic-plastic quasi-conditions, the cohesion (c), internal friction angle (φ), and elastic modulus (E) of the rock and soil mass have the greatest influence on the calculation results). Specifically, when the error between the simulation calculation result and the actual monitoring data was controlled within an allowable range ($P > 0.05$), the physical and mechanical parameters selected for use in the calculation model were considered reasonable. Once validated, the simulation calculations were performed for subsequent working conditions. Figure 7 shows an example of the monitoring data for the displacement of the No. 15 groove wall.

Gradually check the simulation results and horizontal displacement monitoring data of No. 2, 15, 28, and 42 slot sections of diaphragm wall under 2–9 working conditions. Figures 8 and 9 show the verification results of Condition 3 and Condition 6, respectively.

2.3.4. Seepage-Stress Coupling and Process Analysis. The unique temporary nature of foundation pit engineering projects dictates that the force distribution and deformation of the foundation pit supporting structure is not a state problem but rather a process problem. To address the variability of these characteristics between stages of the foundation pit construction process, the process analysis method is proposed and used in this study. Thus, the simulation calculations were divided into three states: no pore water pressure, steady-state seepage, and pore water pressure applied.

Ten working conditions were considered for the no pore water pressure state, as follows:

Condition 0: initial state

Condition 1: construction of underground diaphragm wall

Condition 2: construction of the cap beam and excavation of the first and second layers

Condition 3: construction of the second layer of lining and excavation of the third layer

Condition 4: construction of the third layer of lining and excavation of the fourth layer

Condition 5: construction of the fourth layer of lining and excavation of the fifth layer

Condition 6: construction of the fifth layer of lining and excavation of the sixth layer

Condition 7: construction of the sixth layer of lining and excavation of the seventh layer

Condition 8: construction of the seventh layer of lining and excavation of the eighth layer

Condition 9: construction of the eighth layer of lining and excavation of the ninth layer

Calculation of impose pore water pressure: Conditions 1–9 were considered for the steady-state seepage model. For the model state where pore water pressure was applied, the same conditions were considered. The excavated layer was used to complete the seepage calculations. For example, the excavation of the third layer was used to complete the seepage calculation for Condition 3. A flowchart of the modeling process and analysis is shown in Figure 10.

3. Results

3.1. Determination of Model Parameters. With regards to the selection of model parameters, the underground diaphragm wall and lining parameters were selected according to the design specifications. The Poisson's ratio, gravity, and permeability coefficient were selected according to the results of indoor geotechnical tests. The elastic modulus, friction angle, and cohesive force were simulated and calculated based on field geotechnical test data and subsequently confirmed by the P value inspection method. Table 1 shows the rock and soil simulation parameters checked according to the displacement monitoring data of diaphragm wall under condition 2. Table 2 shows the simulation parameters of foundation pit support structure.

3.2. Analysis of Equivalent Soil Strain. The equivalent plastic strain is an important reference value to measure the plastic deformation of materials. Because of the actual situation of the project and the disturbance of foundation pit excavation to the rock and soil mass, the original strain calculation method is difficult to objectively reflect the strain law of foundation pit soil. In this study, the equivalent plastic

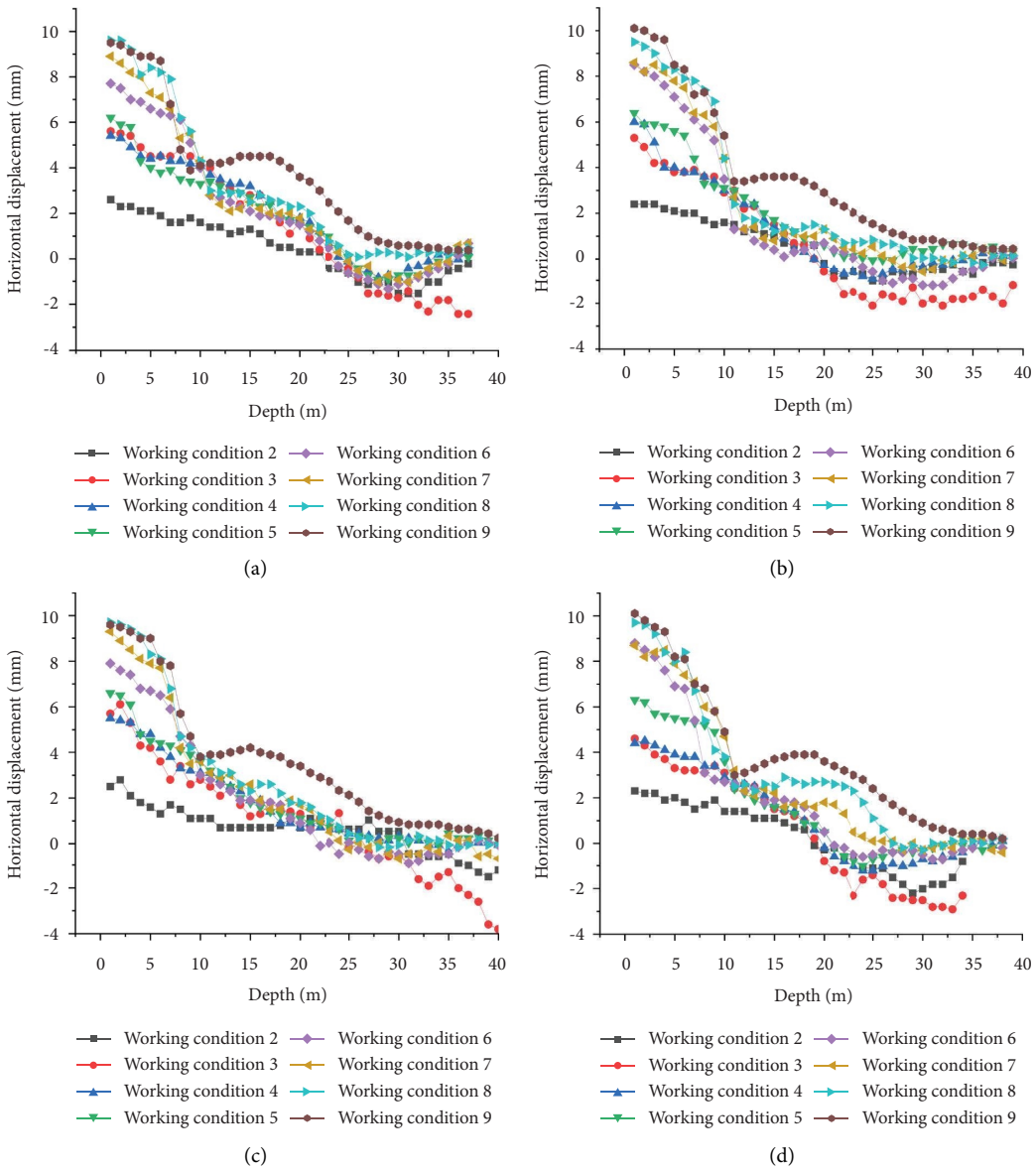

Figure 7: Monitoring data of the underground diaphragm wall. (a) No. 2 section. (b) No. 15 section. (c) No. 28 section. (d) No. 42 section.

strain, which equates the complex strain state of soil to a simple uniaxial tension or compression state, is used to measure the strain characteristics of foundation pit soil. The specific analysis is as follows:

Analysis of Figure 11 shows that the maximum equivalent strain on the foundation pit in working condition 2 (excavation of the second layer) is $7.56959e-3$ (Figure 11(a)) when pore water pressure is not considered. After considering the effects of pore water pressure, the maximum equivalent strain is $7.33992e-3$ (Figure 11(b)). The maximum strain appears near the edge of the bottom of the foundation pit and the strain distribution is circular.

Analysis of Figure 12 shows that the maximum equivalent strain on the foundation pit is $1.13526e-2$ (Figure 12(a)) in working condition 3 (excavation of the third layer) when pore water pressure is not considered. After considering the effects of pore water pressure, the maximum equivalent strain is $1.20842e-2$ (Figure 12(b)). The maximum strain appears near the edge of the bottom of the pit and the strain distribution is similar to that of condition 2.

Analysis of Figure 13 shows that when the pore water pressure is not considered, the maximum equivalent strain of the foundation pit in working condition 4 (excavation of the fourth layer) is $1.37693e-2$ (Figure 13(a)); after considering pore water pressure, the maximum equivalent strain is $1.53166e-2$ (Figure 13(b)). The maximum strain occurs near the edge of the bottom of the pit, and the strain distribution is circular, as in condition 3. However, the equivalent strain distribution changes significantly after considering pore water pressure.

Analysis of Figure 14 shows that the maximum equivalent strain on the foundation pit is $1.53290e-2$ (Figure 14(a)) when pore water pressure is not considered

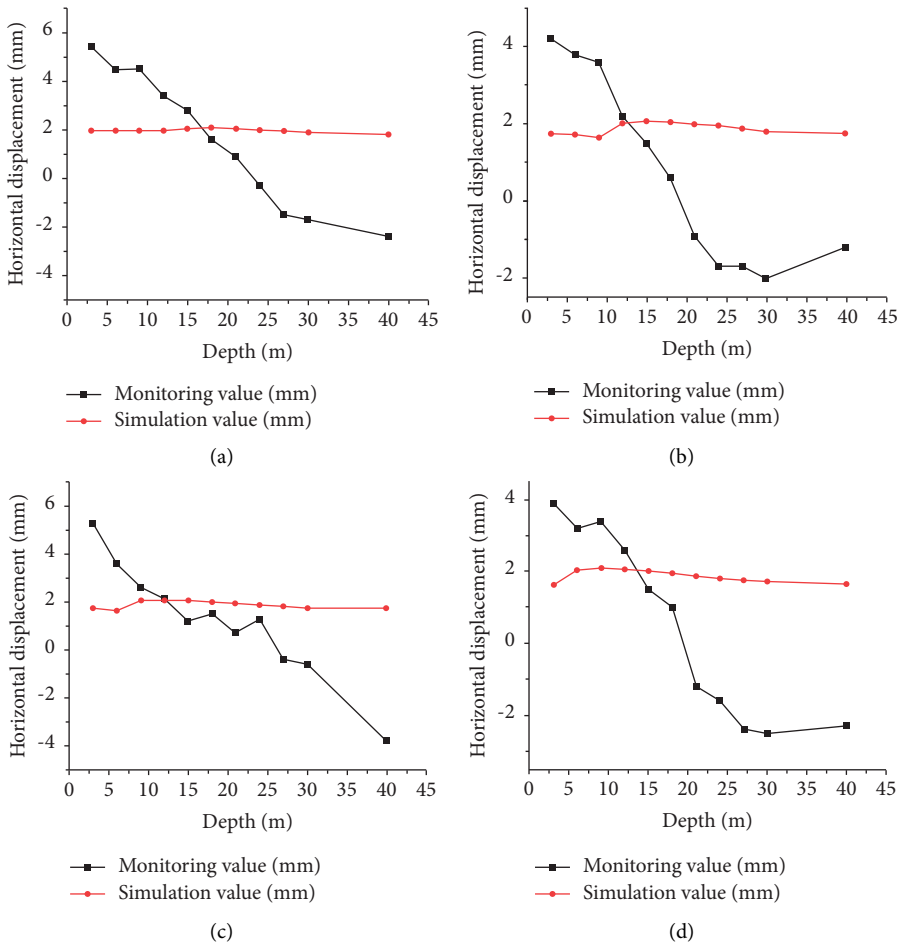

Figure 8: Parameter verification of working condition 3. (a) No. 2 section ($P = 0.63106$). (b) No. 15 section ($P = 0.144479$). (c) No. 28 section ($P = 0.376336$). (d) No. 42 section ($P = 0.095349$).

and $1.73822e-2$ (Figure 14(b)) after considering pore water pressure. The maximum strain occurs near the edge of the bottom of the pit. Similar to working condition 4, the equivalent strain distribution changes significantly after considering the effects of pore water pressure.

Analysis of Figure 15 shows that the maximum equivalent strain on the foundation pit is $1.50441e-2$ (Figure 15(a)) when pore water pressure is not considered and $1.67615e-2$ (Figure 15(b)) when pore water pressure is considered. The maximum strain occurs near the edge of the bottom of the pit. The shape of the equivalent strain area at the bottom of the pit is similar to that of working condition 5.

Analysis of Figure 16 shows that the maximum equivalent strain on the foundation pit is $1.15651e-2$ (Figure 16(a)) when pore water pressure is not considered and $1.25059e-2$ (Figure 16(b)) when pore water pressure is considered. The maximum strain occurs near the edge of the bottom of the pit. The equivalent strain distribution at the bottom of the pit is similar to that of condition 6.

Analysis of Figure 17(a) shows that when pore water pressure is not considered, the maximum equivalent strain on the foundation pit is $4.10912e-4$, which occurs at the junction of the fourth and fifth layers of lining on the sidewall of the foundation pit. Figure 17(b) shows that after considering pore water pressure, the maximum equivalent strain is $7.58077e-4$, which occurs in the middle of the fifth layer of lining on the sidewall of the foundation pit. The strain on the foundation pit wall is significantly increased compared to condition 7, and the equivalent strain distribution changes considerably after considering the effects of pore water pressure.

Analysis of Figure 18(a) shows that when pore water pressure is not considered, the maximum equivalent strain on the foundation pit is $4.47740e-4$, which occurs at the junction of the fifth and sixth layers of lining on the sidewall of the foundation pit. Figure 18(b) shows that after considering the effects of water pressure, the maximum equivalent strain is $8.58466e-4$, which occurs in the middle of the fifth layer of lining on the sidewall of the foundation pit. The distribution of the equivalent strain on the ground surface of the foundation pit is similar to that of condition 8.

Figure 19 shows the variation trend of the equivalent strain maximum value under different working conditions. The maximum equivalent strain on the soil first increases with the excavation of additional layers and then decreases.

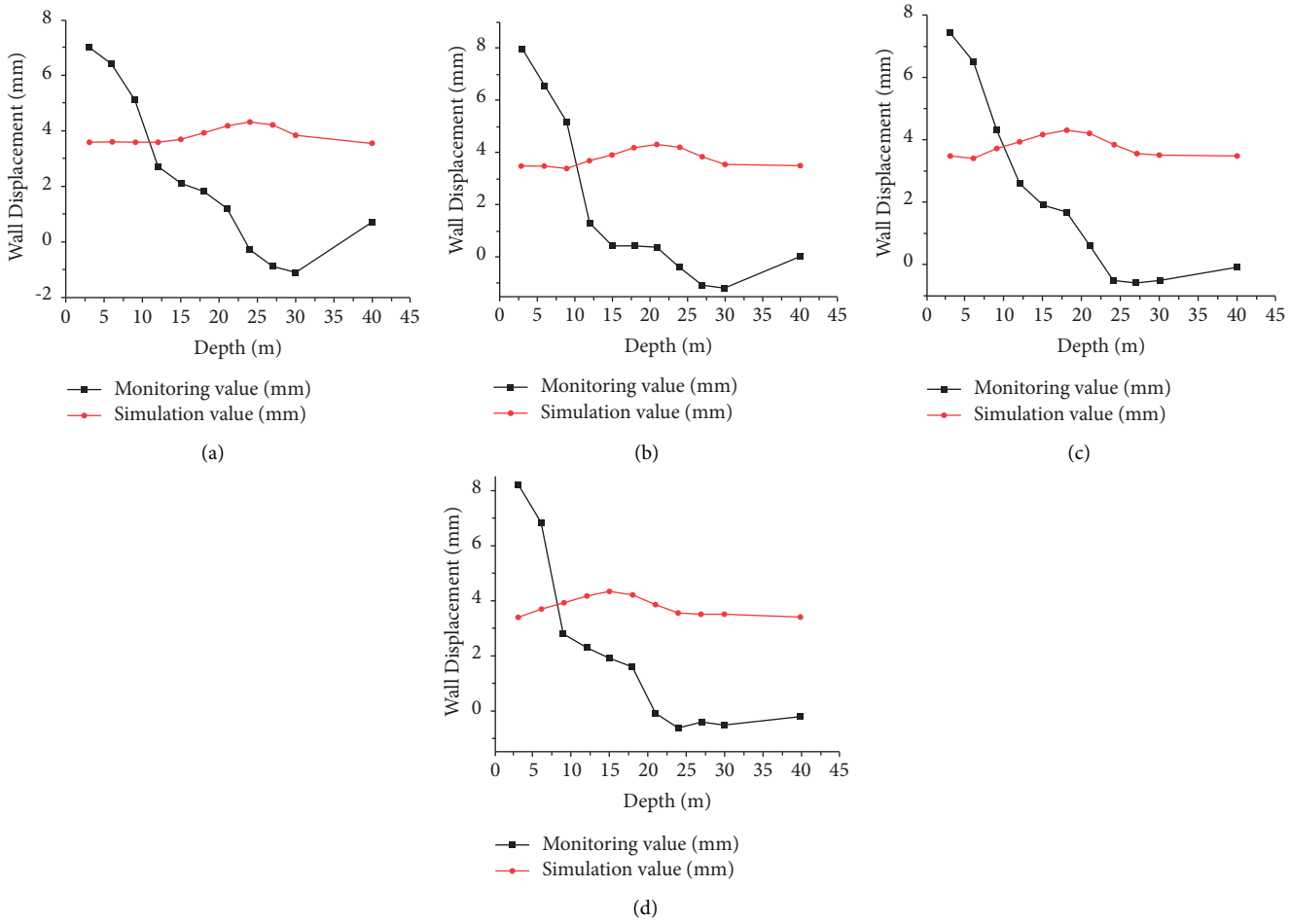

FIGURE 9: Parameter verification of working condition 6. (a) No. 2 section ($P = 0.0793$). (b) No. 15 section ($P = 0.05399$). (c) No. 28 section ($P = 0.066897$). (d) No. 42 section ($P = 0.062761$).

The maximum equivalent strain appears in condition 5 (excavation of the fifth layer). The maximum equivalent strain is relatively small in the excavation of the final layers (conditions 8 and 9). Thus, the excavation of the middle sand layer is critical to the prevention and control of strain on the foundation pit.

The distribution of the maximum equivalent strain in working conditions 5–7 exhibits a "ring mountain" state-a circle of continuous strain distribution with the maximum value occurring approximately 5 m from the edge of the pit bottom. Notably, the equivalent strain area changes significantly before and after considering the effects of pore water pressure in working conditions 4-5.

The location of the maximum equivalent strain in the pit is consistent across working conditions 2–9. After considering pore water pressure, the maximum strain in working condition 2 decreases; however, the maximum strain increased after considering the effects of pore water pressure in all other conditions. The change in equivalent strain after considering the effects of pore water pressure was greatest for working condition 9, with an increase of 91.7%. This suggests that weathered mudstone is sensitive to the effects of pore water pressure.

3.3. Displacement Analysis of Diaphragm Wall. The displacement of diaphragm wall reflects the structural stability characteristics during excavation and support of foundation pit. In order to ensure the safety and controllability of the whole excavation period of the foundation pit, the nephogram analysis is carried out for the displacement of the diaphragm wall:

Analysis of Figure 20 shows that when pore water pressure is not considered, the maximum deformation of the diaphragm wall after the excavation of the first two layers is $1.38685e-3$ m (Figure 20(a)). The maximum deformation occurs at the interface between the first layer and the second layer. The deformation at the edge of the first layer of the underground diaphragm wall is relatively large, consistent with the stress, and deformation characteristics of the cantilever structure. After considering pore water pressure, the maximum deformation of the underground diaphragm wall increased to $7.99612e-3$ m (Figure 20(b)), which occurs at the interface between the fifth and sixth layers that have not yet been excavated (medium sand layer). Affected by the permeability of the sand and pore water pressure, the deformation of the diaphragm wall has a dumbbell-shaped distribution in this case.

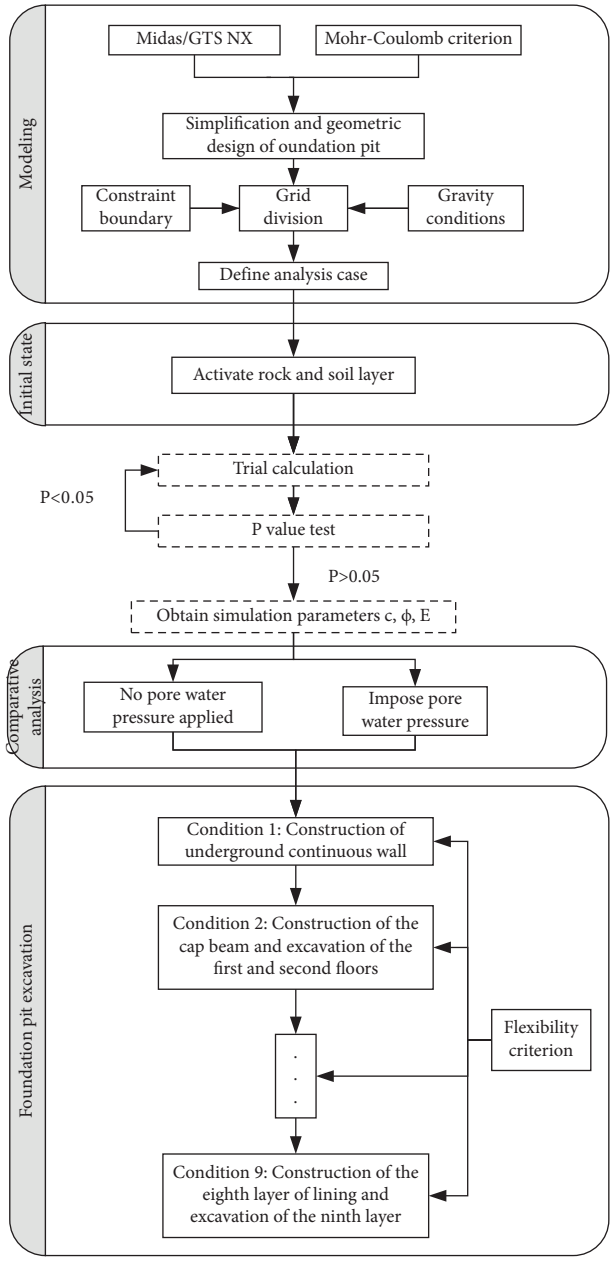

Figure 10: Flowchart of the modeling and calculation process.

Analysis of Figure 21 shows that when pore water pressure is not considered, the maximum value deformation of the diaphragm wall is $2.08474e-3$ m (Figure 21(a)) after the excavation of the third layer. The maximum deformation appears at the interface between the second and third layers. The deformation of the diaphragm wall and the clay contact area (second layer) is relatively large due to the circumferential restraint of the inner lining. After considering the effect of pore water pressure, the maximum deformation of the diaphragm wall increased to $7.47772e-3$ m (Figure 21(b)) and occurs at the interface between the fifth and sixth layers (medium sand layer), which have not yet been excavated. The deformation distribution is similar to condition 2.

Analysis of Figure 22 shows that when pore water pressure is not considered, the maximum deformation of the diaphragm wall after the excavation of the fourth layer is $2.81142e-3$ m (Figure 22(a)) and occurs at the interface between the third and fourth layers. The deformation of the third and fourth layers (silt soil layer) is relatively large because of the circumferential restraint of the inner lining. There is a dumbbell-shaped distribution of deformation. After considering pore water pressure, the deformation of the underground diaphragm wall is extremely large, with a maximum value of $7.29685e-3$ m (Figure 22(b)). The maximum deformation occurs at the interface between the fifth and sixth layers (medium sand layer), which have not yet been excavated. The deformation distribution is similar to condition 3.

Analysis of Figure 23 shows that when pore water pressure is not considered, the maximum deformation of the diaphragm wall is $3.55944e-3$ m (Figure 23(a)) after the excavation of the fifth layer. The maximum deformation appears at the interface between the silt soil layer (fourth layer) and the middle sand soil layer (fifth layer). After considering the effects of pore water pressure, the maximum deformation of the diaphragm wall is $7.63439e-3$ m (Figure 23(b)) and occurs at the interface between the fifth and sixth layers. The deformation distribution is similar to condition 4.

Analysis of Figure 24 shows that when pore water pressure is not considered, the maximum deformation of the diaphragm wall is $4.30336e-3$ m (Figure 24(a)) after the excavation of the sixth layer. The maximum deformation occurs at the interface between the silt soil (fourth layer) and middle sand soil layers (fifth layer). The deformation of the underground diaphragm wall is relatively large at the fourth and fifth layers. The deformation distribution of the underground diaphragm wall is similar to condition 5. After considering pore water pressure, the maximum deformation of the diaphragm wall is $8.26873e-3$ m (Figure 24(b)), which occurs at the interface between the fifth and sixth layers. The deformation distribution is similar to condition 5.

Analysis of Figure 25 shows that when pore water pressure is not considered, the maximum deformation of the diaphragm wall is $4.88058e-3$ m (Figure 25(a)) after the excavation of the seventh layer. The maximum deformation occurs at the interface between the silt soil and middle sand soil layers. After considering pore water pressure, the maximum deformation increases to $8.80627e-3$ m (Figure 25(b)), which occurs at the interface between the fifth and sixth layers. The deformation distribution is similar to condition 6.

Analysis of Figure 26 shows that when pore water pressure is not considered, the maximum deformation of the diaphragm wall is $5.39555e-3$ m (Figure 26(a)) after the excavation of the eighth layer. This occurs at the interface of the fifth and sixth layers. After considering pore water pressure, the maximum deformation of the diaphragm wall is $9.14792e-3$ m (Figure 26(b)), which occurs at the interface between the fifth and sixth layers. The deformation distribution is similar to condition 7.

Table 1: Summary of relevant soil parameters.

Soil layers	Elastic modulus (kN/m^2)	Poisson's ratio	Friction angle (°)	Cohesion (kN/m^2)	Natural heavy (kN/m^3)	Permeability coefficient (cm/s)
Silt	3000	0.30	3	5	15.4	$1.15e-6$
Muddy soil	50000	0.27	5	8	16.5	$1.18e-6$
Fine sand	80000	0.23	18	0	19.0	$5.01e-3$
Medium sand	120000	0.24	25	0	19.5	$1.21e-2$
Coarse sand	200000	0.22	28	0	18.8	$3.12e-2$
Strong weathered mudstone	500000	0.19	20	50	19.9	$1.02e-4$
Middle weathered mudstone	1000000	0.17	30	450	20.5	$1.14e-5$
Microweathered mudstone	1400000	0.15	35	600	20.7	$9.71e-7$

Table 2: Structural parameters and mechanical parameters.

Structures	Elastic modulus (kN/m^2)	Weight (kN/m^3)	Poisson's ratio
Underground diaphragm wall	3.07*E*7	25	0.2
Lining	3.07*E*7	25	0.2

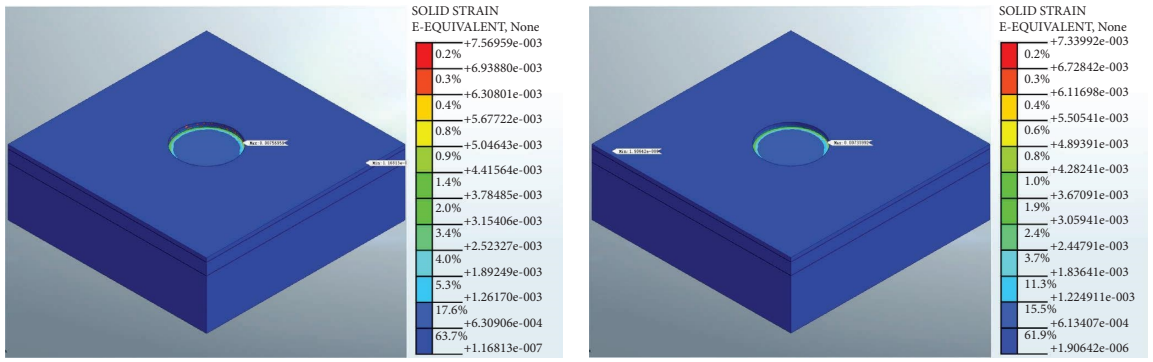

(a) (b)

Figure 11: Working condition 2. Equivalent soil strain (a) without pore water pressure and (b) with pore water pressure applied.

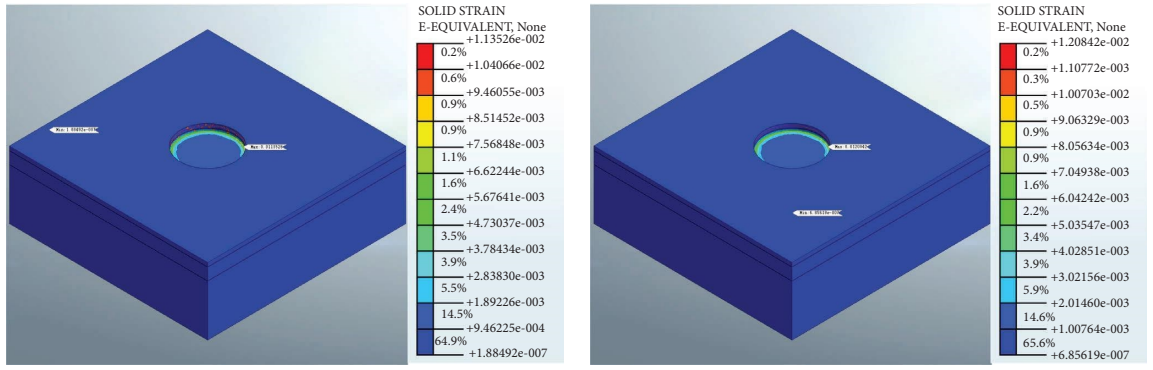

(a) (b)

Figure 12: Working condition 3. Equivalent soil strain (a) without pore water pressure and (b) with pore water pressure applied.

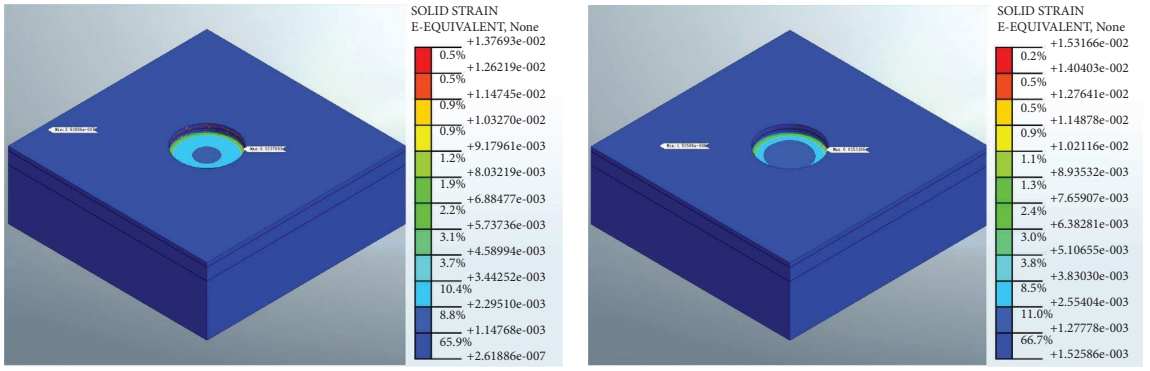

(a) (b)

Figure 13: Working condition 4. Equivalent soil strain (a) without pore water pressure and (b) with pore water pressure applied.

Analysis of Figure 27 shows that when pore water pressure is not considered, the maximum deformation of the diaphragm wall is $5.79305e-3$ m (Figure 27(a)) after the excavation of the ninth layer. The maximum deformation occurs at the interface of the fifth and sixth layers. After considering pore water pressure, the maximum deformation

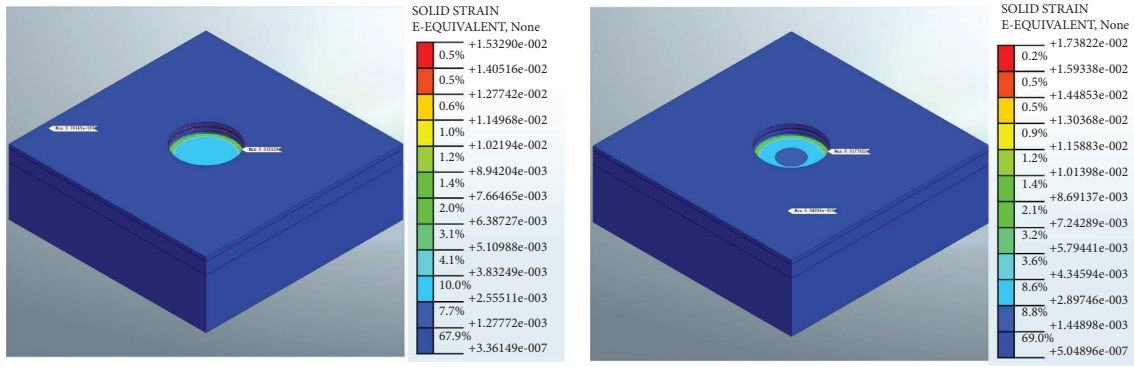

(a) (b)

Figure 14: Working condition 5. Equivalent soil strain (a) without pore water pressure and (b) with pore water pressure applied.

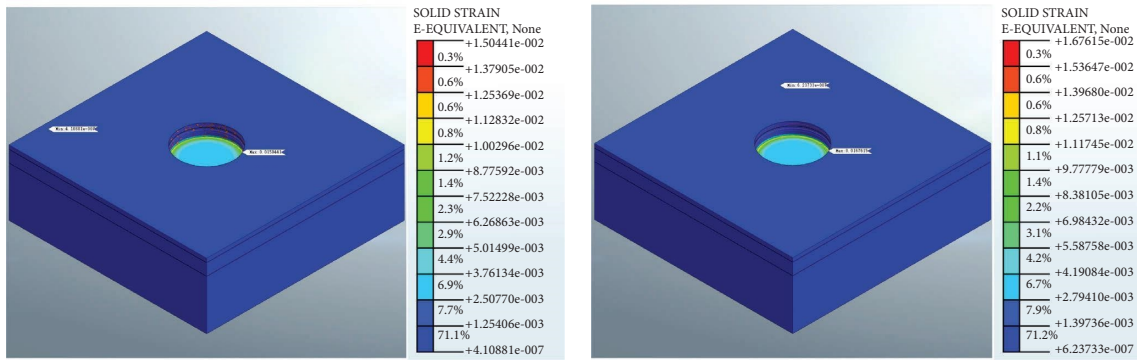

(a) (b)

Figure 15: Working condition 6. Equivalent soil strain (a) without pore water pressure and (b) with pore water pressure applied.

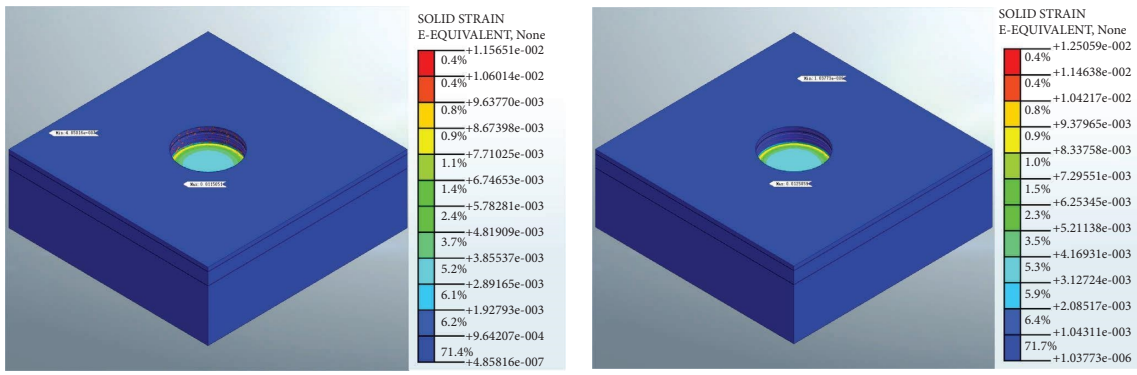

(a) (b)

Figure 16: Working condition 7. Equivalent soil strain (a) without pore water pressure and (b) with pore water pressure applied.

of the diaphragm wall is $9.81842e-3$ m (Figure 27(b)), which occurs at the interface of the fifth and sixth layers. The deformation distribution is similar to condition 8.

Analysis of Figure 28 shows that when pore water pressure is not applied, the maximum deformation of the diaphragm wall increases linearly as more layers of the foundation pit are excavated. Furthermore, the site of the maximum deformation gradually moves from the interface of the first and second layers to the interface of the fifth and sixth layers. When considering the effects of pore water pressure, the maximum deformation of the diaphragm wall first decreases and then increases with the excavation of additional layers. The maximum deformation is consistently located at the interface between the fifth and sixth foundation pit layers, even when considering the conditions before these layers have been excavated. Accordingly, the middle sand layers (the fifth and sixth foundation pit layers) are critical to preventing and controlling the deformation of the diaphragm wall.

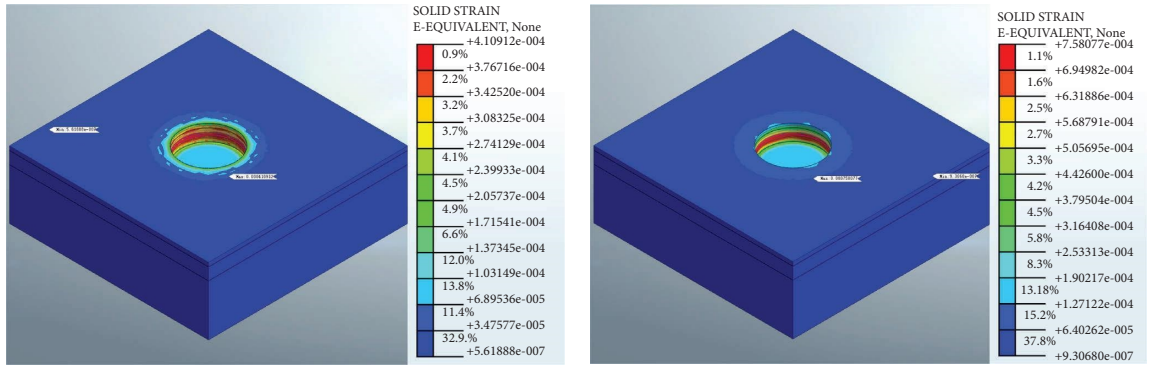

(a) (b)

Figure 17: Working condition 8. Equivalent soil strain (a) without pore water pressure and (b) with pore water pressure applied.

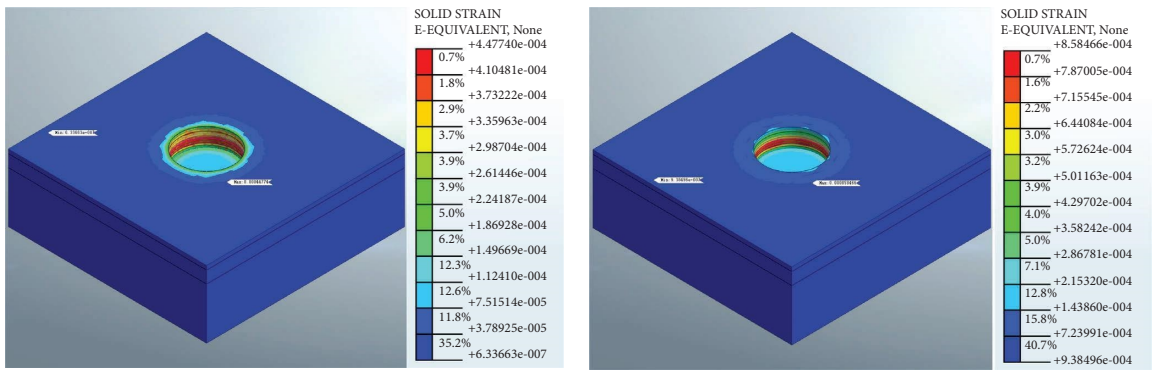

(a) (b)

Figure 18: Working condition 9. Equivalent soil strain (a) without pore water pressure and (b) with pore water pressure applied.

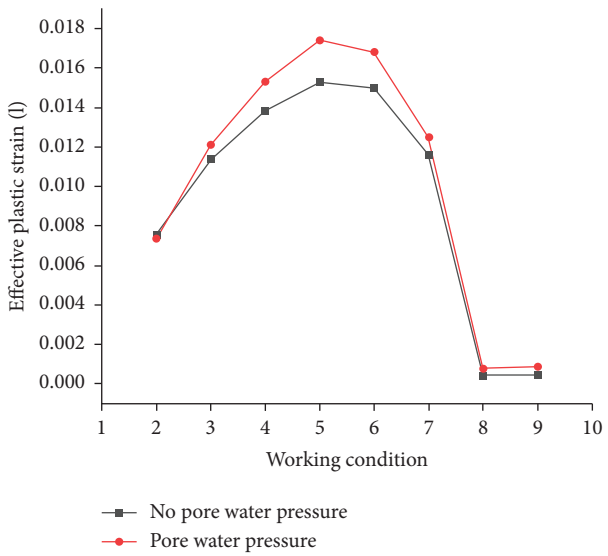

Figure 19: Maximum equivalent soil strain with and without pore water pressure applied.

With regards to the deformation distribution, the underground diaphragm wall deformation exhibits a dumbbell-shaped distribution by working condition 9, both with and without pore water pressure applied. However, this deformation distribution gradually evolves as the excavation progresses when ignoring the effects of pore water pressure. Conversely, this distribution is consistent across all considered conditions when pore water pressure is applied.

In summary, there are significant changes in the maximum deformation and the deformation distribution after considering the effects of pore water pressure in working conditions 2–7. Specifically, the maximum deformation in each working condition increases after considering pore water pressure; the increase in working condition 2 is the greatest, with a 4.77-fold change. This result shows that pore water pressure has a significant effect on the deformation of the diaphragm wall.

3.4. Analysis of the Axial Force on the Inner Pit Lining. This study also explored the effect of pore water pressure on the axial force of the foundation pit lining.

Analysis of Figure 29 shows that when pore water pressure is not considered, the maximum absolute liner axial force on the inner lining is $-8.34491e2$ kN (Figure 29(a)) after the excavation of the first and second foundation pit layers. After considering pore water pressure, the maximum absolute liner axial force is $-3.33002e2$ kN (Figure 29(b)). The site of the maximum axial force is consistent between conditions (Figures 29(a) and 29(b)).

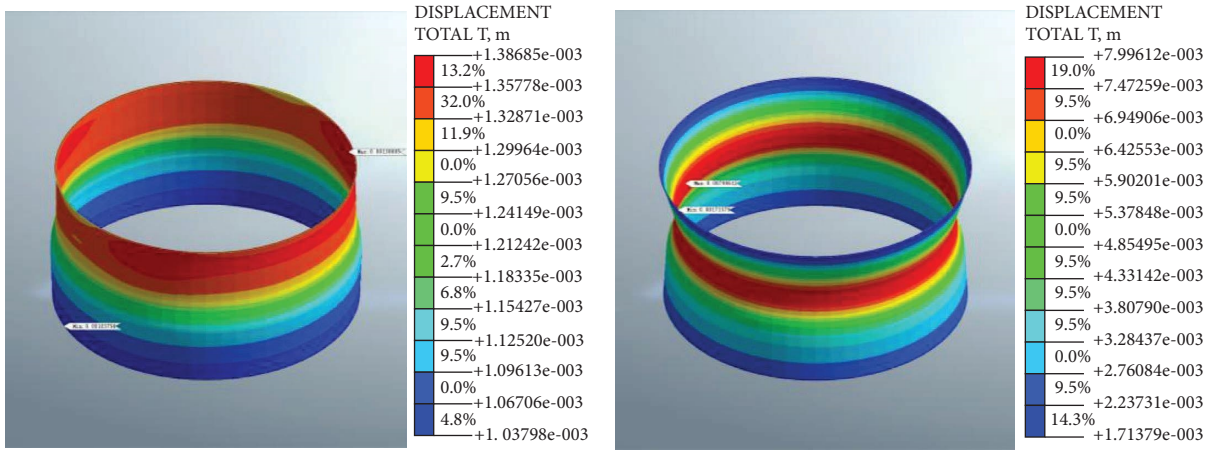

(a) (b)

Figure 20: Working condition 2 wall deformation (a) without pore water pressure and (b) with pore water pressure applied.

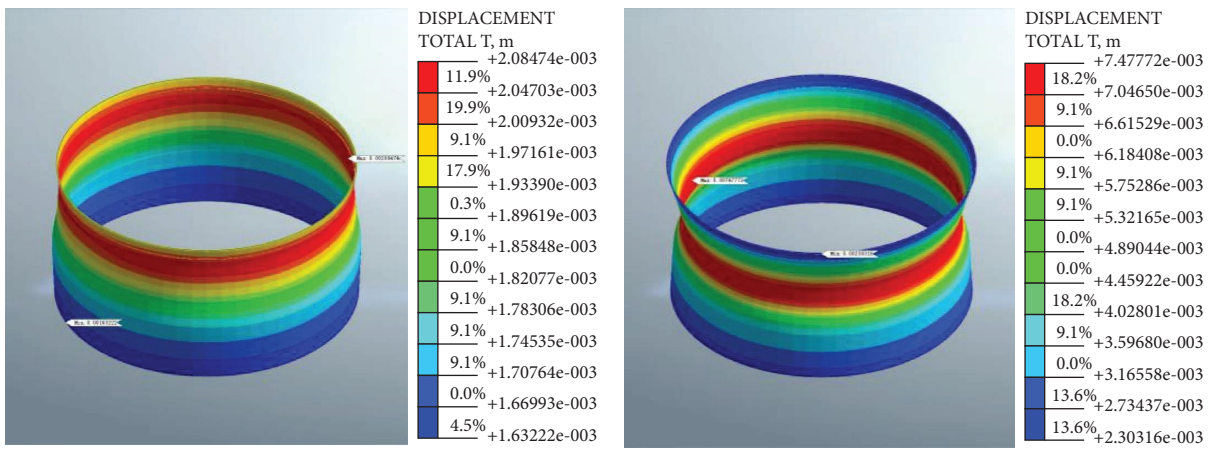

(a) (b)

Figure 21: Working condition 3 wall deformation (a) without pore water pressure and (b) with pore water pressure applied.

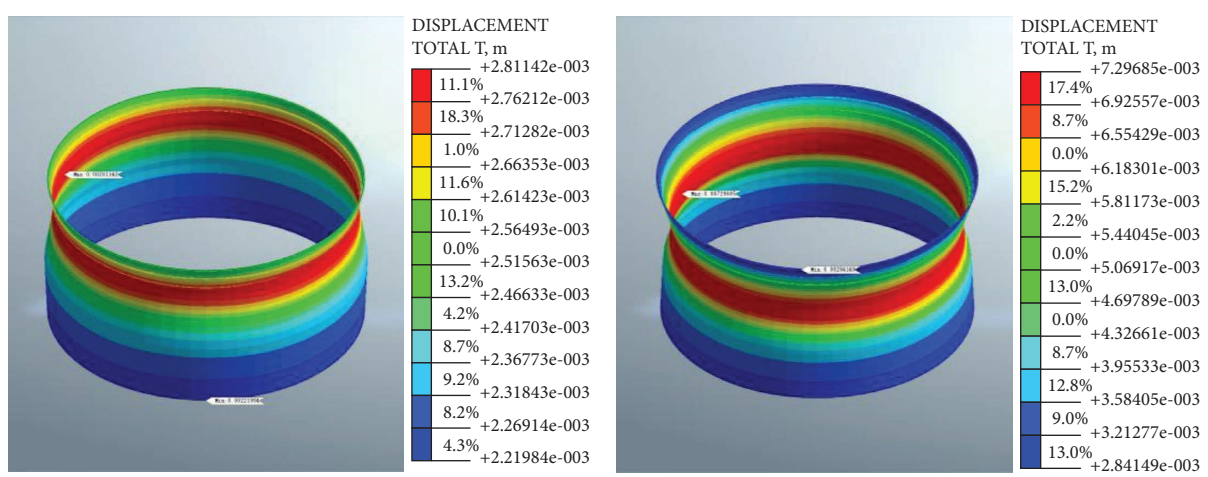

(a) (b)

Figure 22: Working condition 4 wall deformation (a) without pore water pressure and (b) with pore water pressure applied.

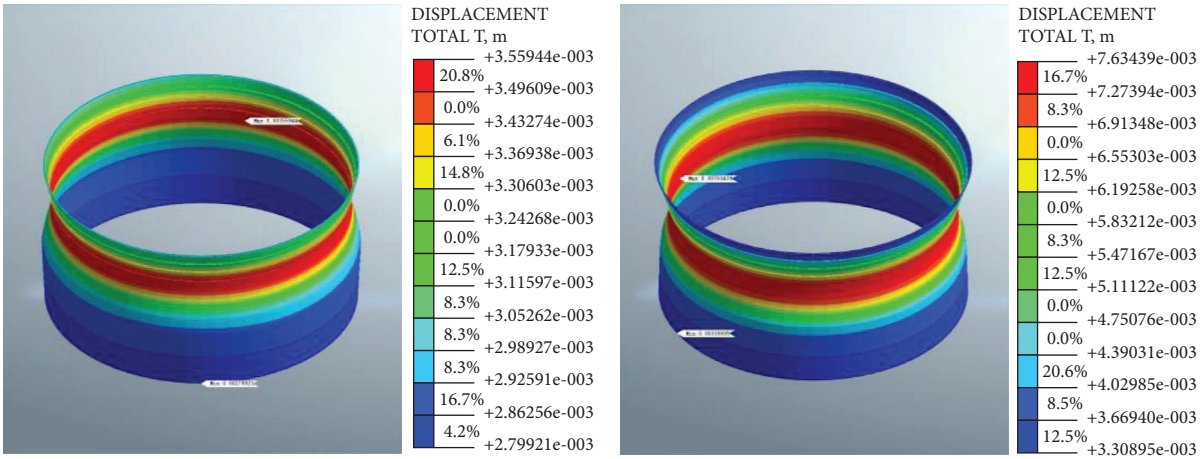

(a) (b)

Figure 23: Working condition 5 wall deformation (a) without pore water pressure and (b) with pore water pressure applied.

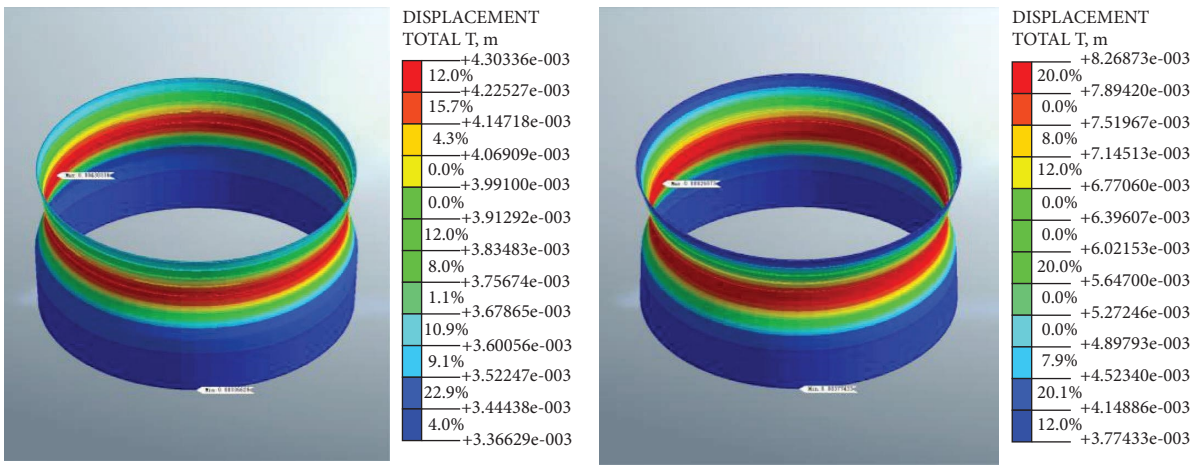

(a) (b)

Figure 24: Working condition 6 wall deformation (a) without pore water pressure and (b) with pore water pressure applied.

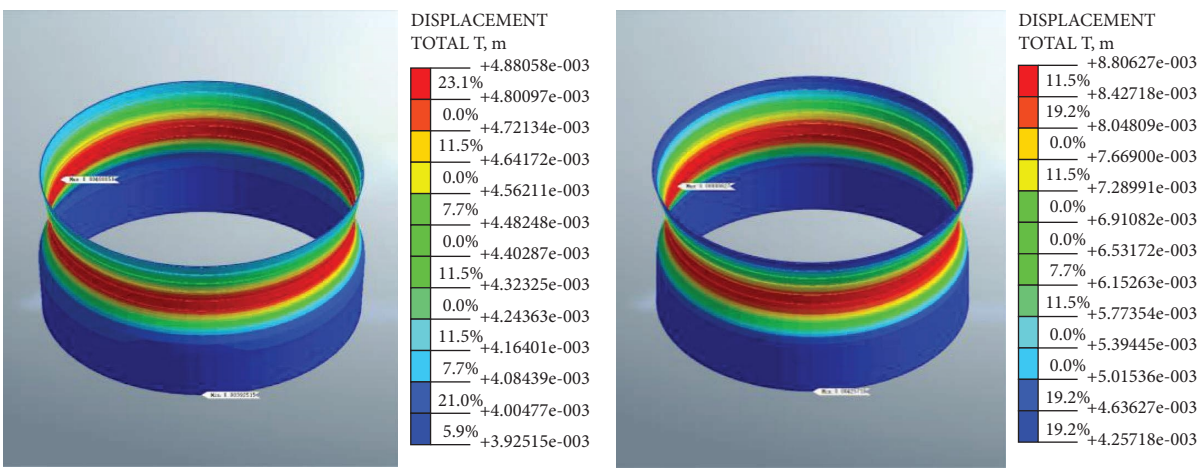

(a) (b)

Figure 25: Working condition 7 wall deformation (a) without pore water pressure and (b) with pore water pressure applied.

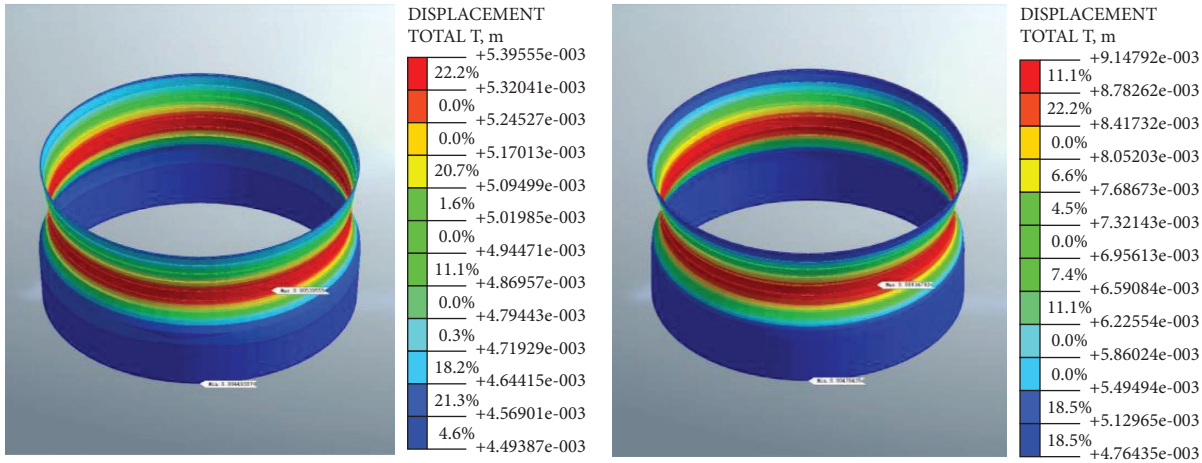

(a) (b)

Figure 26: Working condition 8 wall deformation (a) without pore water pressure and (b) with pore water pressure applied.

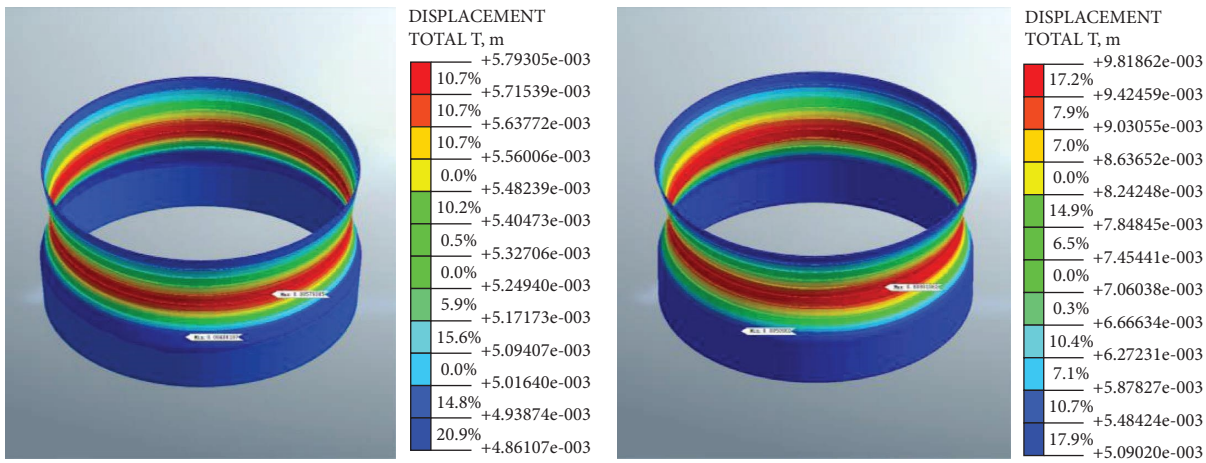

(a) (b)

Figure 27: Working condition 9 wall deformation (a) without pore water pressure and (b) with pore water pressure applied.

Analysis of Figure 30 shows that when pore water pressure is not considered, the maximum absolute liner axial force on the inner pit lining is $-1.02039e3$ kN (Figure 30(a)) after the excavation of the third layer of the pit. After considering pore water pressure, the maximum absolute liner axial force is $-7.31029e2$ kN (Figure 30(b)). There is a significant change in the location of the maximum linear axial force after applying pore water pressure.

Analysis of Figure 31 shows that when pore water pressure is not considered, the maximum absolute liner axial force on the inner lining is $-9.19388e2$ kN (Figure 31(a)) after the excavation of the fourth layer of the pit. After considering the effect of pore water pressure, the maximum absolute liner axial force is $-8.35253e2$ kN (Figure 31(b)). There is a significant change in the location of the maximum axial force after applying pore water pressure.

Analysis of Figure 32 shows that when pore water pressure is not considered, the maximum absolute liner axial force on the inner lining is $-1.06719e3$ kN (Figure 32(a)) after the excavation of the fifth layer. After applying pore water pressure, the maximum absolute liner axial force is $-7.56661e2$ kN (Figure 32(b)). The location of the maximum liner axial force changes significantly after applying pore water pressure. Furthermore, the distribution of the axial force changes compared to the previous conditions. Specifically, the axial force on the inner lining increases from top to bottom, and the axial force on the newly constructed (fourth) layer of the inner lining is obviously greater than the first three layers.

Analysis of Figure 33 shows that when pore water pressure is not considered, the maximum absolute liner axial force on the inner lining is $-1.28114e3$ kN (Figure 33(a)) after the excavation of the sixth layer. After considering pore water pressure, the maximum absolute liner axial force is $-9.65728e2$ kN (Figure 33(b)). The location of the maximum axial force changes significantly after considering the effects of pore water pressure. Similar to working condition 5, the axial force on the lining increases from top to bottom, and

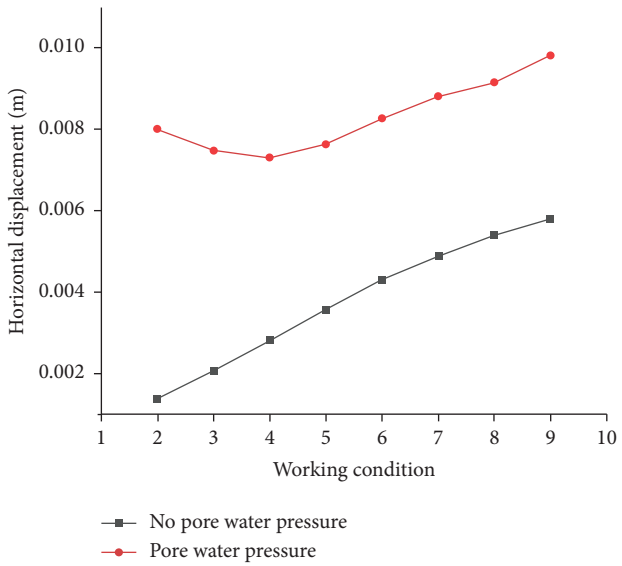

Figure 28: Maximum deformation of the underground diaphragm wall.

the axial force on the newly constructed lining (fifth layer) is significantly greater than the force on the first four layers.

Analysis of Figure 34 shows that when pore water pressure is not considered, the maximum absolute liner axial force on the pit lining is −1.4719*e*3 kN (Figure 34(a)) after the excavation of the seventh layer. After considering pore water pressure, the maximum absolute liner axial force is −1.12127*e*3 kN (Figure 34(b)). The location of the maximum linear axial force changes significantly after considering the effects of pore water pressure. Similar to the previous conditions, the axial force on the lining increases from top to bottom, and the axial force on the newly constructed lining (sixth layer) is significantly greater than that on the first five layers.

Analysis of Figure 35 shows that when pore water pressure is not considered, the maximum absolute liner axial force on the lining is −1.4692*e*3 kN (Figure 35(a)) after the excavation of the eighth layer. After considering the effects of pore water pressure, the maximum absolute liner axial force is −1.15220*e*3 kN (Figure 35(b)). As in the previous conditions, the location of the maximum linear axial force changes significantly after considering the effects of pore water pressure. Furthermore, the axial force of the inner lining increases from top to bottom, and the axial force on the newly constructed inner lining (the seventh layer) is significantly greater than that on the first six layers.

Analysis of Figure 36 shows that when pore water pressure is not considered, the maximum absolute liner axial force on the inner lining is −1.54989*e*3 kN (Figure 36(a)) after the excavation of the ninth layer. After considering pore water pressure, the maximum absolute liner axial force is −2.50205*e*3 kN (Figure 36(b)). After considering pore water pressure, the location of the maximum liner axial force changes significantly. Furthermore, as in previous conditions, the axial force on the lining increases from top to bottom, and the axial force on the newly constructed lining (the eighth layer) is significantly greater than that on the first seven layers.

As shown in Figure 37, the maximum liner axial force on the pit lining increases significantly as foundation pit excavation progresses. The maximum liner axial force occurs in the eighth layer of the lining after the excavation of the ninth layer of the foundation pit. In working conditions 5–9, the axial force on the inner lining increases from the top to the bottom of the pit, and the axial force on the newly constructed layer of the inner lining is greater than that on the layers constructed in previous stages. Thus, the newly constructed layer of lining is a sensitive location for liner axial force monitoring.

The distribution of the linear axial force is similar regardless of whether pore water pressure is considered. However, the location of the maximum liner axial force changes after applying pore water pressure for working conditions 4–9. Furthermore, compared with the deformation of the underground diaphragm wall, the lining axial force is less affected by the excavation rock and soil conditions.

The maximum liner axial force decreases in working conditions 2–8 when considering pore water pressure, with a maximum decrease of 60.1% in working condition 2. However, the maximum axial force increases by 61.4% in working condition 9 after considering pore water pressure. Thus, pore water pressure has a significant effect on the axial force on the foundation pit lining.

4. Discussion

This study relies on the excavation and support engineering of the west anchorage pit of Humen Second Bridge. A new method for checking simulation parameters based on the monitoring data of diaphragm wall displacement is proposed. The modeling calculation and analysis theory of foundation pit excavation and support process is established. A method of superimposing pore water pressure to realize seepage-stress coupling is proposed. The stress and deformation characteristics of the soil layer and the supporting structure during the excavation and supporting process of the foundation pit are obtained as follows:

The maximum equivalent strain of the foundation pit first increases and then decreases with the excavation conditions (the peaks in conditions 5-6). During the excavation of the foundation pit, the maximum equivalent strain has a unique "ring-shaped mountain" distribution in working conditions 5–7. Considering the influence of pore water pressure, the maximum equivalent strain change is the largest in the excavation of the ninth layer of foundation pit, which increases by 91.7%. It shows that the weathered mudstone is very sensitive to the influence of pore water pressure.

During the excavation of the foundation pit, the deformation of the diaphragm wall and the maximum axial force of the lining tend to increase. After considering the effect of pore water pressure, the location and distribution of the maximum deformation of the underground diaphragm wall changed significantly. In addition, the excavation of the intermediate sand layer is essential to prevent and control the deformation of the diaphragm wall. The distribution of the deformation of the diaphragm wall is "dumbbell shape."

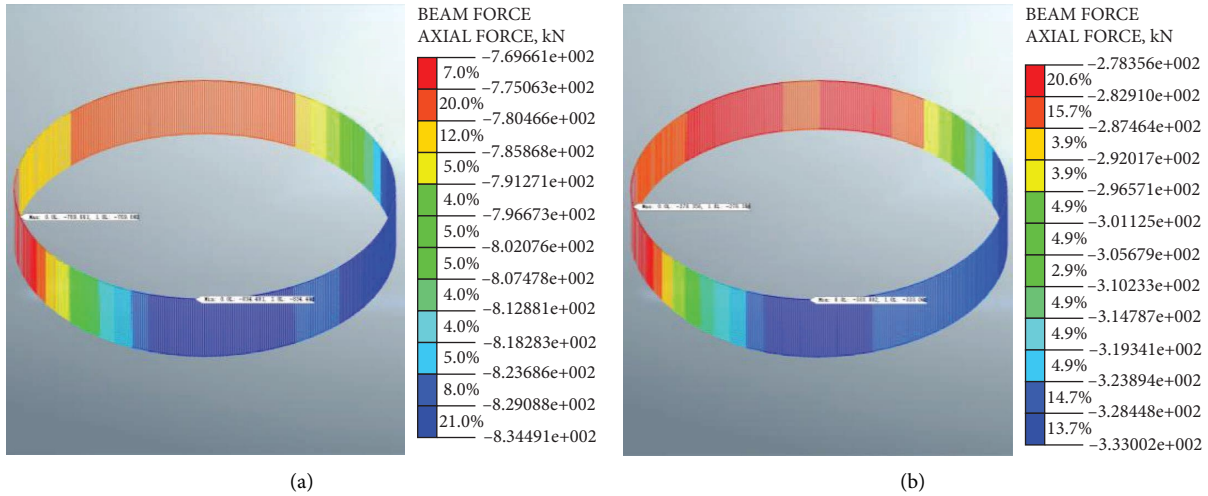

(a) (b)

Figure 29: Working condition 2 lining axial force (a) without pore water pressure and (b) with pore water pressure applied.

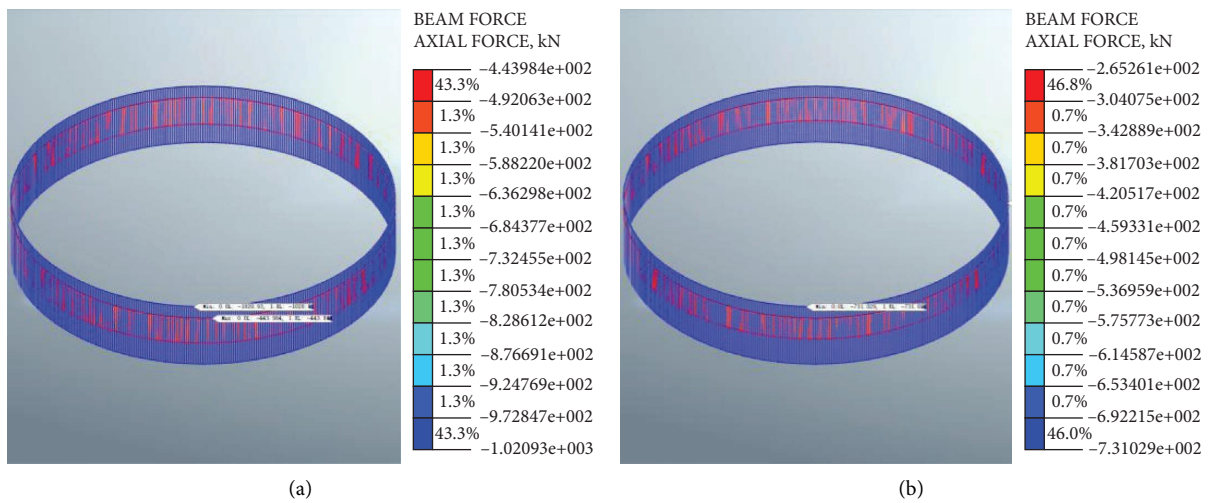

(a) (b)

Figure 30: Working condition 3 lining axial force (a) without pore water pressure and (b) with pore water pressure applied.

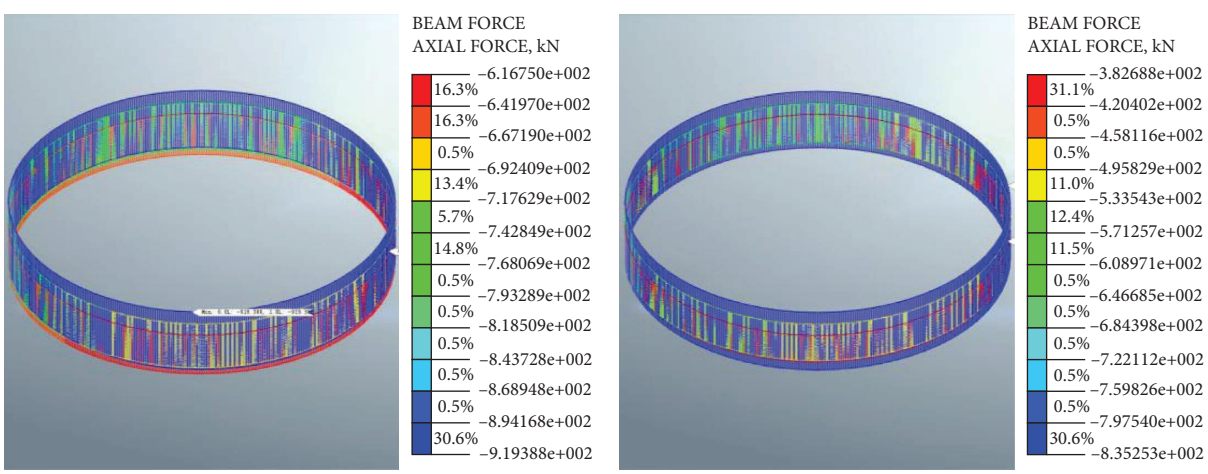

(a) (b)

Figure 31: Working condition 4 lining axial force (a) without pore water pressure and (b) with pore water pressure applied.

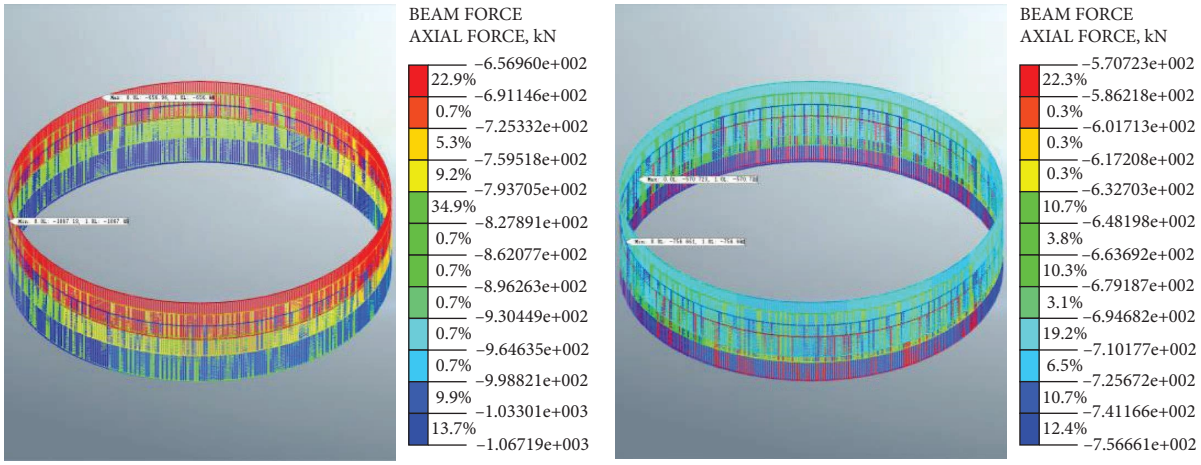

(a) (b)

Figure 32: Working condition 5 lining axial force (a) without pore water pressure and (b) with pore water pressure applied.

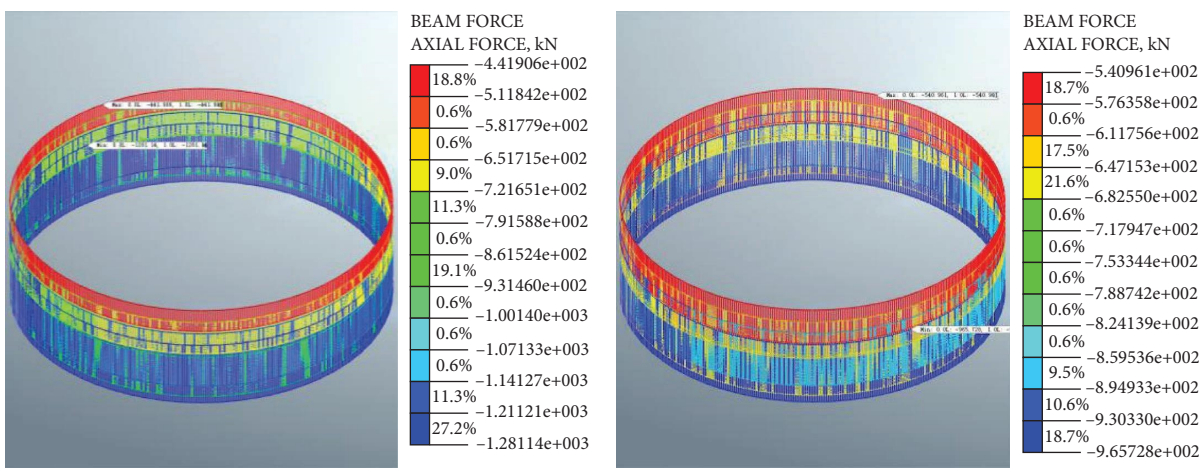

(a) (b)

Figure 33: Working condition 6 lining axial force (a) without pore water pressure and (b) with pore water pressure applied.

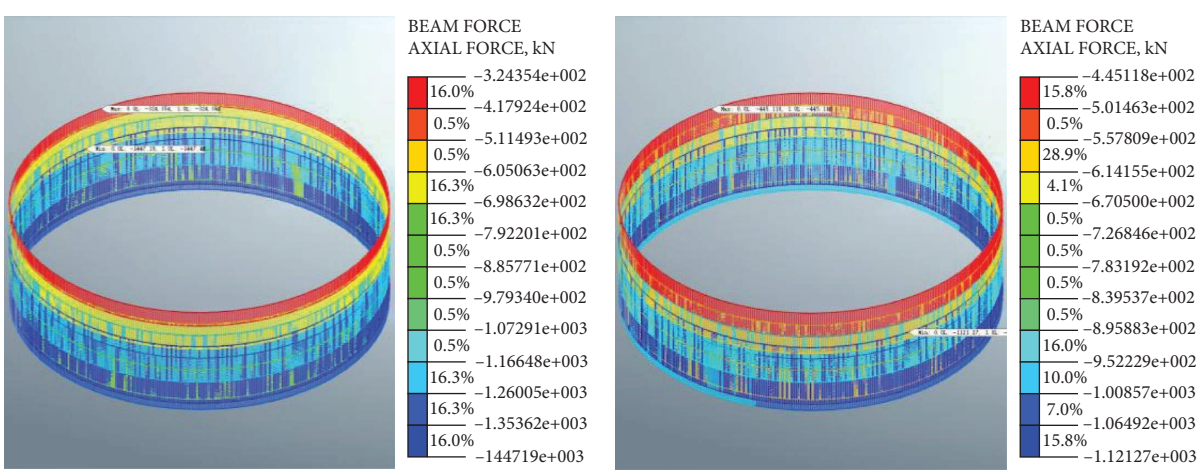

(a) (b)

Figure 34: Working condition 7 lining axial force (a) without pore water pressure and (b) with pore water pressure applied.

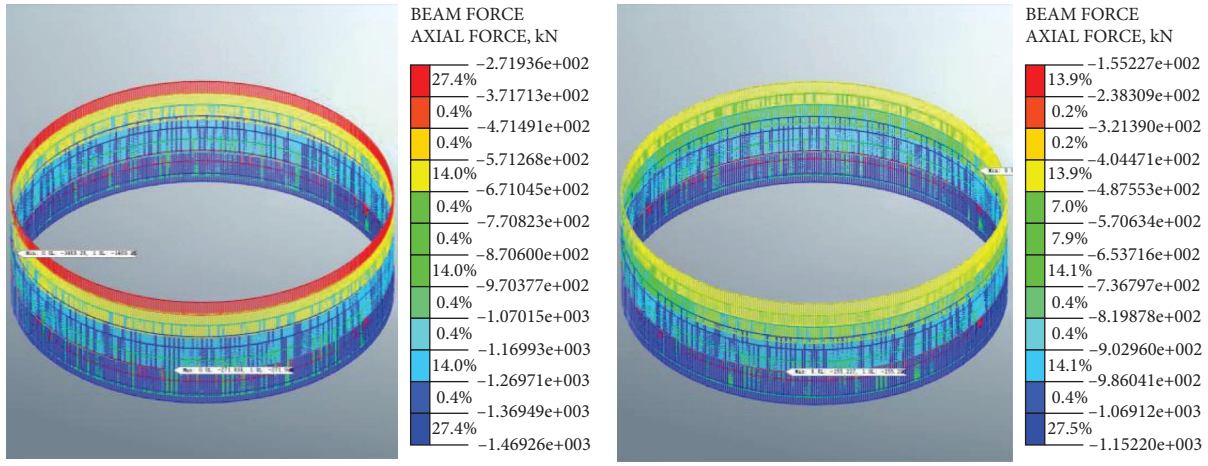

Figure 35: Working condition 8 lining axial force (a) without pore water pressure and (b) with pore water pressure applied.

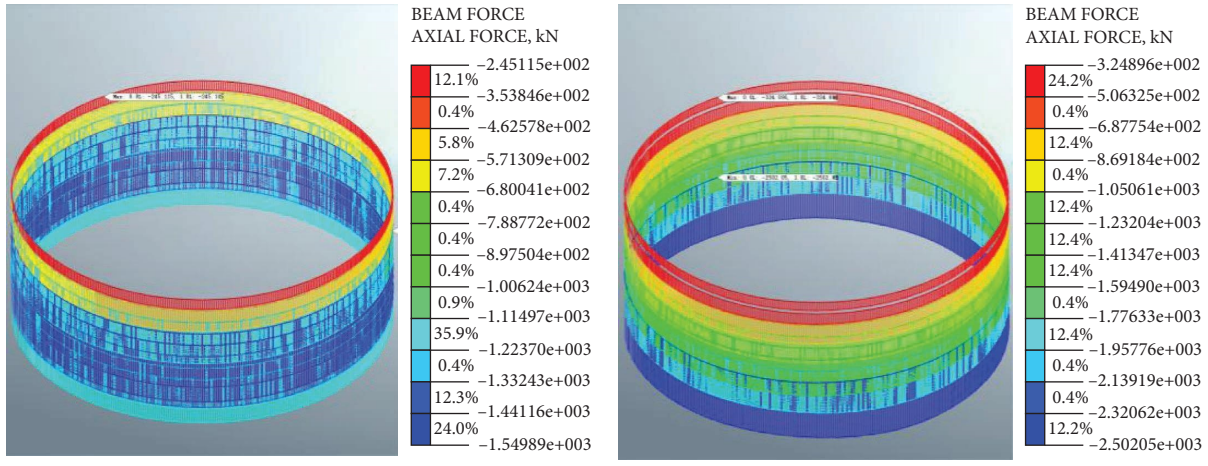

Figure 36: Working condition 9 lining axial force (a) without pore water pressure and (b) with pore water pressure applied.

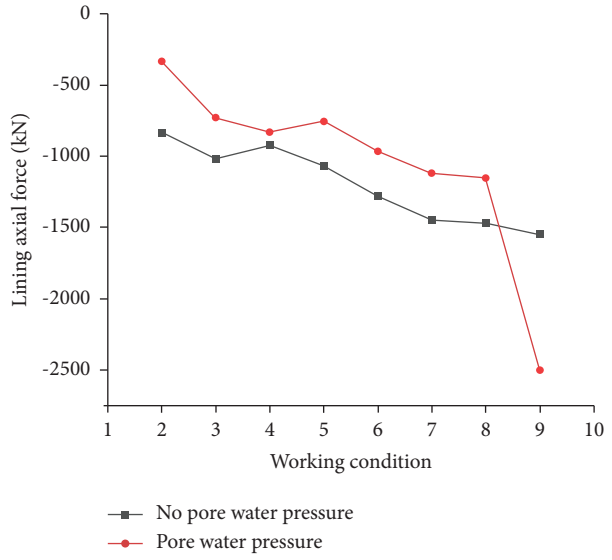

Figure 37: Maximum liner axial force on the foundation pit lining across conditions.

The deformation of the diaphragm wall changes after considering the pore water pressure. In 5–9 working conditions, the axial force of the lining increases from top to bottom. After applying pore water pressure, the deformation of the diaphragm wall after excavation of the second layer increased by 4.77 times compared with the state without pore water pressure. However, the pit lining axial force was reduced by 60.1%. In most cases, the pore water pressure reduces the deformation of the diaphragm wall, while the pore water pressure increases the axial force on the excavation lining.

5. Conclusion

This study proposes an analysis method for the excavation support process. Combined with the simulation parameter checking method based on monitoring data, the stress and deformation analysis of the supporting structure during the excavation of the foundation pit is carried out. The early warning analysis of circular foundation pit excavation in sandy soil layer is realized.

The stress-seepage coupling is realized based on the superposition calculation method of pore water pressure. The stress and deformation characteristics of the diaphragm wall and lining under steady seepage conditions are analyzed. The stress-deformation response mechanism of the support structure during the excavation of the circular foundation pit in the sandy soil layer is revealed.

The process analysis method proposed in this study is also applicable to the numerical simulation of geotechnical engineering such as foundation pit excavation, slope support, and karst settlement. Although this method can realize the full-cycle simulation of the project, however, it still relies heavily on field monitoring data, especially the parameter calibration of initial operating conditions.

Data Availability

The data used to support the findings of this study are available from the corresponding author upon reasonable request.

Disclosure

This manuscript has not been published or presented elsewhere in part or in entirety and is not under consideration by another journal.

Conflicts of Interest

The authors declare that they have no conflicts of interest.

Acknowledgments

This work was supported by the National Key R&D Program of China (grant number 2022YFC3002600); the National Natural Science Foundation of China (grant number 51708043); the Observation and Research Station of Ground Fissure and Land Subsidence, Ministry of Natural Resources (grant number 2022-03); the Natural Science Basic Research Plan in Shaanxi Province of China (grant numbers 2019JQ-680 and 2022JQ-358); and the Special Fund for Basic Scientific Research of Central Colleges (Natural Sciences) (grant numbers 300102219209 and D5000210117).

References

[1] K. Y. Kim, D. S. Lee, J. Cho, S. S. Jeong, and S. Lee, "The effect of arching pressure on a vertical circular shaft," *Tunnelling and Underground Space Technology*, vol. 37, no. 6, pp. 10–21, 2013.

[2] Y. Tan and D. L. Wang, "Structural behaviors of large underground earth-retaining systems in shanghai. I: unpropped circular diaphragm wall," *Journal of Performance of Constructed Facilities*, vol. 29, no. 2, Article ID 04014058, 2015.

[3] G. Wu, W. Chen, H. Bian, and J. Yuan, "Structure optimisation of a diaphragm wall with special modelling methods in a large-scale circular ventilating shaft considering shield crossing," *Tunnelling and Underground Space Technology*, vol. 65, pp. 35–41, 2017.

[4] G. Q. Zhao, Y. Y. Yang, and S. Y. Meng, "Failure of circular shaft subjected to hydraulic uplift: field and numerical investigation," *Journal of Central South University*, vol. 27, no. 1, pp. 256–266, 2020.

[5] H. Faheem, F. Cai, and K. Ugai, "Three-dimensional base stability of rectangular excavations in soft soils using FEM," *Computers and Geotechnics*, vol. 31, no. 2, pp. 67–74, 2004.

[6] G.-L. Dai, W.-M. Gong, X.-Q. Zhou, Y.-Z. Liu, and L.-J. Liu, "Experiment and analysis on horizontal bearing capacity of single- chamber closed diaphragm wall," *Journal of Building Structures*, vol. 33, pp. 67–73, 2012.

[7] H.-X. Wang, "Influence of excavation width on enclosure-structure stability of foundation pits," *China Civil Engineering Journal*, vol. 44, pp. 120–126, 2011.

[8] J. L. Borges and G. T. Guerra, "Cylindrical excavations in clayey soils retained by jet grout walls: numerical analysis and parametric study considering the influence of consolidation," *Computers and Geotechnics*, vol. 55, pp. 42–56, 2014.

[9] J. Cho, H. Lim, S. Jeong, and K. Kim, "Analysis of lateral earth pressure on a vertical circular shaft considering the 3D arching effect," *Tunnelling and Underground Space Technology*, vol. 48, pp. 11–19, 2015.

[10] A. Chehadeh, A. Turan, and F. Abed, "Numerical investigation of spatial aspects of soil structure interaction for secant pile wall circular shafts," *Computers and Geotechnics*, vol. 69, pp. 452–46110, 2015.

[11] T. Schwamb and K. Soga, "Numerical modelling of a deep circular excavation at Abbey Mills in London," *Géotechnique*, vol. 65, no. 7, pp. 604–619, 2015.

[12] A. Chehadeh, A. Turan, F. Abed, and M. Yamin, "Lateral earth pressures acting on circular shafts considering soil-structure interaction," *International Journal of Geotechnical Engineering*, vol. 13, no. 2, pp. 139–151, 2017.

[13] Y. S. Xu, S. L. Shen, L. Ma, W. J. Sun, and Z. Y. Yin, "Evaluation of the blocking effect of retaining walls on groundwater seepage in aquifers with different insertion depths," *Engineering Geology*, vol. 183, pp. 254–264, 2014.

[14] Y. X. Wu, S. L. Shen, H. N. Wu, Y. S. Xu, and W. J. Yin, "Environmental protection using dewatering technology in a deep confined aquifer beneath a shallow aquifer," *Engineering Geology*, vol. 196, pp. 59–70, 2015.

[15] Q. L. Cui, S. L. Shen, Y. S. Xu, H. N. Wu, and Z. Y. Yin, "Mitigation of geohazards during deep excavations in karst

regions with caverns: a case study," *Engineering Geology*, vol. 195, pp. 16–27, 2015.

[16] Y. Q. Zhang, M. G. Li, J. H. Wang, J. J. Chen, and Y. F. Zhu, "Field tests of pumping-recharge technology for deep confined aquifers and its application to a deep excavation," *Engineering Geology*, vol. 228, pp. 249–259, 2017.

[17] Y. Cai, B. Hao, C. Gu, J. Wang, and L. Pan, "Effect of anisotropic consolidation stress paths on the undrained shear behavior of reconstituted wenzhou clay," *Engineering Geology*, vol. 242, pp. 23–33, 2018.

[18] Y.-L. Li, B. Chen, C.-C. Ma, and B.-P. Zhou, "Analysis of excavation slope under rainfall infiltration basing on ABAQUS," *Chinese Journal of Applied Mechanics*, vol. 34, pp. 155–161, 2017.

[19] T. Schwamb, K. Soga, R. J. Mair et al., "Fibre optic monitoring of a deep circular excavation," *Proceedings of the Institution of Civil Engineers-Geotechnical Engineering*, vol. 167, no. 2, pp. 144–154, 2014.

[20] N. E. Faustin, M. Z. E. B. Elshafie, and R. J. Mair, "Case studies of circular shaft construction in London," *Proceedings of the Institution of Civil Engineers-Geotechnical Engineering*, vol. 171, no. 5, pp. 391–404, 2018.

[21] B. T. Le, R. J. Goodey, and S. Divall, "Subsurface ground movements due to circular shaft construction," *Soils and Foundations*, vol. 59, no. 5, pp. 1160–1171, 2019.